Astron. Astrophys. 347, 684–695 (1999)

ASTRONOMY AND ASTROPHYSICS

X-ray and radio manifestations of a solar eruptive event

N. Gopalswamy[1], **N. Nitta**[2], **P.K. Manoharan**[3], **A. Raoult**[4], **and M. Pick**[4]

[1] Department of Physics, The Catholic University of America, Washington DC and NASA/GSFC, Greenbelt, MD 20771, USA
[2] Lockheed Martin Advanced Technology Center, Building 252, Department H1-12, 3251 Hanover Street, Palo Alto, CA 94304, USA
[3] Radio Astronomy Center, TIFR, Ooty, India
[4] Meudon Observatory, Section A'Astrophysique, 5 Place Jules Janssen, F-92195 Meudon Principal Cedex, Paris, France

Received 17 July 1998 / Accepted 8 April 1999

Abstract. We report on a study of the changes in the vicinity of a disappearing solar filament (DSF) that occurred on 1993 April 30. The DSF was associated with a long duration X-ray event (LDE) observed by the GOES and Yohkoh spacecraft. A detailed analysis of the X-ray images obtained by the Yohkoh Soft X-ray Telescope revealed that X-ray manifestations of the eruption were wide-spread: (i) X-ray enhancement over a coronal volume several times larger than that of the eruption region, probably the X-ray counterpart of a coronal mass ejection (CME), (ii) X-ray ejecta accelerating to 670 km s^{-1} into the corona, and (iii) quasi-stationary X-ray loops as in long decay events (LDEs) were observed. One of the important findings of this study is the large-scale X-ray enhancement which we identify with the frontal structure of a CME, apart from the well-known X-ray ejecta and post-eruption arcade formation. There is evidence for triggering of a sympathetic flare in an adjoining active region due to the X-ray ejecta from the eruption region. Stationary metric radio continuum observed by the Nançay Radioheliograph was found to be associated with the brightest X-ray loops that formed following the filament eruption. The unpolarized continuum radio emission was found to be bremsstrahlung radiation from the hot plasma observed in X-rays. The event was also associated with a low frequency metric type II radio burst due to a coronal shock wave from the eruption region. The onset time of the type II emission precludes the possibility of a CME-driven shock causing it. Although we do not have positional information for the type II burst, we found that the X-ray ejecta was fast enough to drive the coronal shock. We confirmed this by comparing the speed of the X-ray ejecta with the shock speed obtained from the radio data which agreed within 10%.

Key words: Sun: corona – Sun: filaments – Sun: flares – Sun: radio radiation – Sun: X-rays, gamma rays

1. Introduction

The sudden disappearances of solar filaments, also known as disparition brusques (DBs), can be dynamic (the filament erupts) or thermic (the filament is heated but does not erupt). It has become increasingly clear that the dynamic DBs can serve as useful proxies to Earth-bound coronal mass ejections (CMEs). Apart from their prediction value for space weather forecast (Joselyn & McIntosh, 1981), the DBs provide vital information to understand the formation and destruction of the filaments (see e.g. Wagner, 1986). The thermic DBs are one of the best examples of varying temperature structure of the filament environment (Mouradian et al. 1986). During a thermic DB, the dark filament can disappear in Hα while appearing in EUV because of heating by irradiance of overlying hot loops, while maintaining the overall shape and structure. While thermic DBs are important in understanding the physics, the dynamic DBs are potentially geo-effective, because of the ejected material and the associated coronal dynamics. It may be possible that a filament undergoing thermic DB may eventually undergo dynamic DB, because of the structural changes caused during the former event. We need observations at other wavelengths such as EUV and X-rays to decide whether an eruption occurs during a DB.

The CMEs originating on the solar disk cannot be observed in white light until they are quite far away from the surface because of the way in which white light coronagraphs operate. Thus we need to resort to radio, EUV and X-ray observations to determine the near surface manifestations of CMEs (Gopalswamy et al., 1996; 1997a,b; Hudson & Webb, 1997; Gopalswamy & Hanaoka, 1998; Gopalswamy et al., 1998a). Since eruptive filaments are often found as the core of CMEs, the dynamic DBs may also tell us about the CME onset. Dynamic DBs can result in fast ejecta that are associated with metric type II and type IV radio bursts (Gopalswamy et al., 1997b). The type II radio bursts are caused by coronal shock waves while the type IV bursts are produced by energetic electrons trapped in stationary or moving structures. Radio observations at metric wavelengths provide important information at intermediate heights: the shock waves and plasmoids can be effectively detected within about a solar radius from the DSF site in order to understand what ultimately leaves the Sun in addition to the CME and what is left behind. Furthermore, the metric radio bursts of type II are important in deciding which one of the many CME substructures drive the shock. We had an opportunity to look into some of these aspects of the 1993 April 30 DSF event. This study has confirmed some of our previous results on

Send offprint requests to: N. Gopalswamy

X-ray signatures of CMEs and coronal shock sources and has provided new insight into the filament eruption process.

2. Observational results

2.1. The filament disappearance

The dark filament in question was located on the disk between N00E10 and S10E30 at 08:40 UT (1993 April 30) and was bowed in the NE direction (see Fig. 1a). The filament separated the positive and negative polarity regions of an extended plage located to the east of the disk center. The filament was reported to be active for several hours prior to its disappearance starting around 1350 UT (Solar Geophysical Data, April 1993) A gradual C1.0 GOES X-ray flare started around 13:30 UT in association with the DSF and continued for several hours. Fig. 1b is a Hα image taken after the DSF. Weak ribbon structures can be seen at 14:10 UT on either side of the initial location of the filament. We also see small-scale brightening to the left of the filament. This probably was a pre-flare brightening associated with a Hα subflare reported to be starting, peaking and ending at 14:18, 14:19 and 14:28 UT respectively. The Hα flare occurred in AR 7494 located at the eastern end of the large-scale plage region in question. The flare occurred where a parasitic positive polarity was found in the surrounding negative polarity. AR 7494 was a newly emerging region. Note that the Hα flare is from the compact region AR 7494 while the GOES flare is associated with the whole DSF.

In Fig. 1c, we have shown the large-scale X-ray structure overlying the filament as observed by Yohkoh mission's Soft X-ray Telescope (SXT, Tsuneta et al., 1991). The X-ray image taken after the DSF (Fig. 1d) shows complex loop brightenings following the eruption of the overlying structures. The longitudinal component of the photospheric magnetic field in the vicinity of the DSF in Fig. 1e shows the overall magnetic connectivity in the region. The He 10830 Å image in Fig. 1f confirms the weak post-eruption ribbon structure seen in the Hα image.

2.2. Metric type II burst and radio continuum

At metric wavelengths, a type II burst with fundamental-harmonic structure was observed by the Nançay Decametric Array. The harmonic component of the burst started around 14:27 UT near 72 MHz and drifted to lower frequencies with a rate of ~ 0.11 MHz s^{-1}. The harmonic component was very prominent compared to the fundamental so we shall use it for quantitative calculations. A starting frequency of 72 MHz means that the coronal shock responsible for the type II burst must have formed only at a height where the local plasma frequency was 36 MHz, corresponding to a density of $1.6\times\ 10^7$ cm^{-3}. The observing frequencies of the Nançay radioheliograph are much higher than the starting frequency of the type II burst and so there is no positional information. There was no type III radio burst associated with this event, suggesting that energetic electrons accelerated during the event did not have access to open magnetic field lines.

There was no other report of metric radio emission from any of the radio observatories. However, when we examined the Nançay radioheliograph data, we found a weak unpolarized continuum radio emission at 164 MHz starting from about 14:25 UT with a peak around 14:34 UT. The radio emission was much weaker at 216 MHz and was absent at higher frequencies. The lowest observing frequency of the Nançay Radioheliograph is 164 MHz and so we do not know if the continuum was present at lower frequencies. The centroids of the continuum radio source were clearly associated with the eruption region (see below).

2.3. Details of the eruption in soft X-rays

The eruptive event was well observed by Yohkoh/SXT. Both full frame images (FFI) and partial frame images (PFI) of AR 7494 were obtained. The FFIs were obtained in thin aluminum and sandwich filters with a time resolution of $\sim$ 2 min. The PFIs were obtained in thick and thin aluminum filters with a time resolution of about 8 s. The PFIs were centered around AR 7494 in the 5.2 arc min $\times$ 5.2 arc min field of view and contain information on the Hα flare and related mass motions. Most of the activity in soft X-rays was in the vicinity of the DSF region, including AR 7494. In addition, there was a weak X-ray enhancement on a much larger scale around the DSF region. We believe that this is the X-ray signature of the frontal structure of a coronal mass ejection (CME). We shall describe these observations in the following two subsections.

2.3.1. X-ray activity in the DSF region

Fig. 2 shows the evolution of X-ray structures associated with the DSF region. Three stages of the eruption could be identified in soft X-rays. The earliest hint of activity in X-rays was the disappearance of the pre-event structures A and B in Fig. 2b around 13:32 UT. It is difficult to quantify the motion of the structure B, but when the X-ray images are displayed as movies, one could see that the structure moved vertically with a possible northward tilt. One can also notice a general sense of 'opening' of the large-scale corona in the vicinity. This may be the X-ray signature of a CME. We shall come back to this point later. In the second stage, thin long loops resembling the filament erupted and moved out. The direction of motion of these loops were slightly inclined to the direction of eruption in the early stage. The bright loops seemed to move to the north and east. We call these bright loops as X-ray ejecta. These ejecta seem to be axial (loops follow the curve of the underlying neutral line) similar to the ones reported in other studies (Sheeley et al., 1975; Kahler, 1977; McAllister et al., 1992; Solberg & McAllister, 1998; Khan et al., 1997). The arrows in Fig. 2d-g point to one of the fast moving large-scale loop structures. This structure seems to span the entire DSF region and can be seen lifting off during the interval 14:08 to 14:18 UT. In Fig. 2h, this is too faint to see. When the bright loop was moving out, a number of stationary loops brightened apparently in the vicinity of the original location of the filament and started rising very slowly. Fig. 2e shows many X-ray loops involved in the event. These

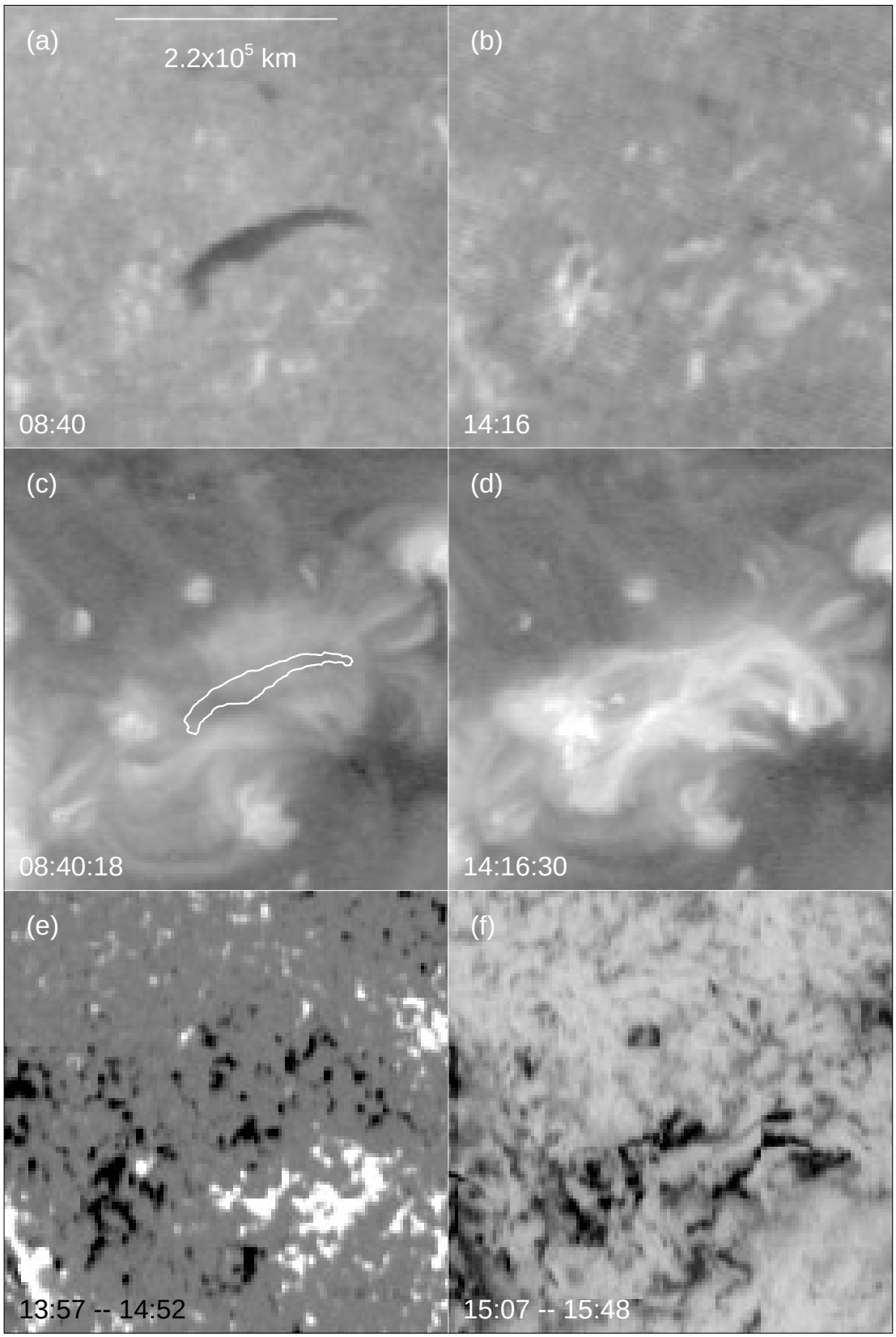

Fig. 1a–f. Overview of the eruptive event. **a** and **b** Hα images (from the Solar Observing Optical Network) at 08:40 and 14:16 UT corresponding to times before and after the DSF. **c** Pre-event X-ray arcade (gray scale) overlying the filament (contour overlay); **d** Complex X-ray loop structure at 14:16:30 UT after the DSF; **e** Kitt Peak magentogram (longitudinal) showing the connectivity in the region of interest (dark for negative polarity and white for positive polarity) and **f** the same region in Kitt Peak He 10830 after the DSF. The scale of the images is marked in **a**.

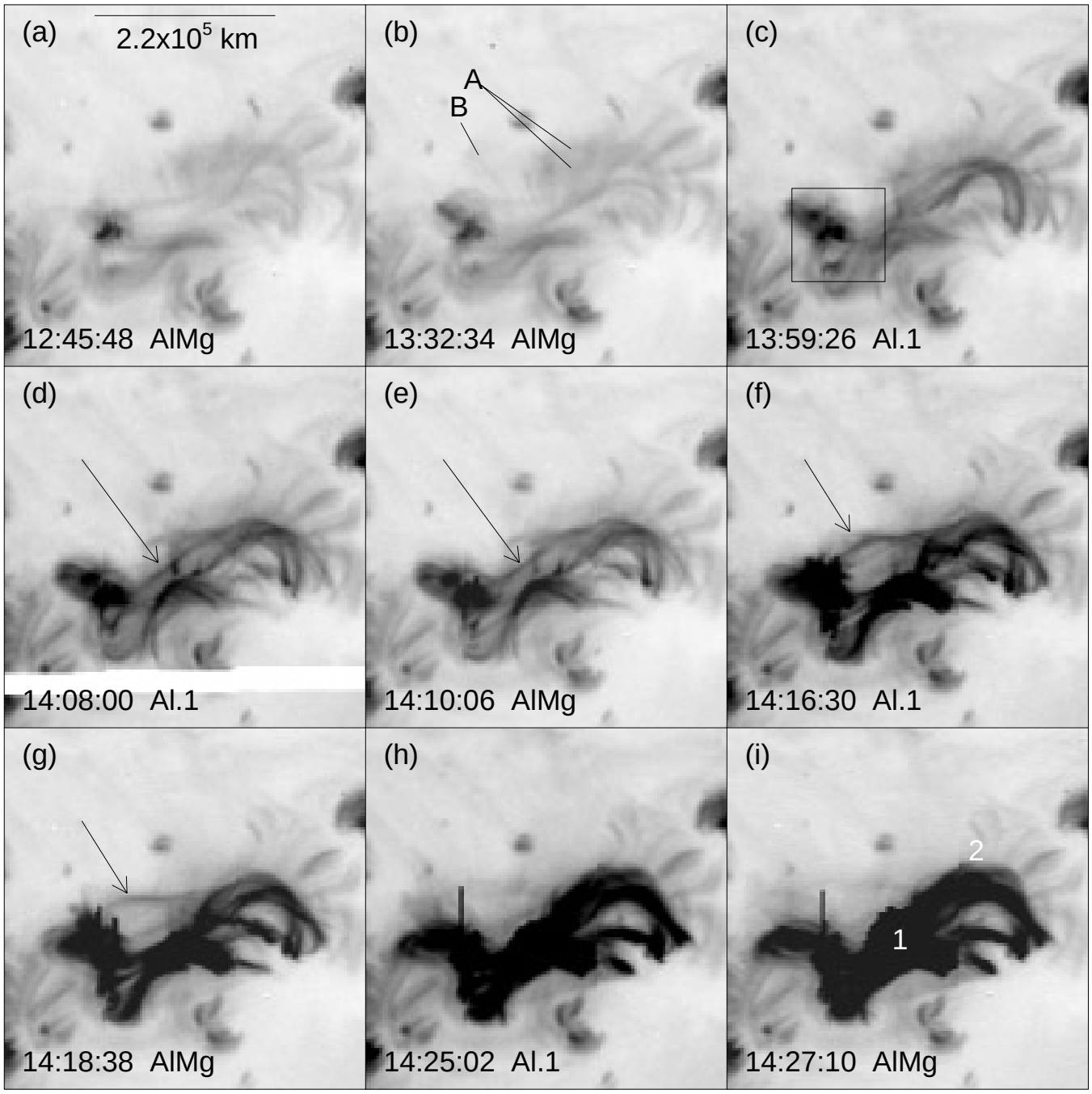

Fig. 2a–i. evolution of the X-ray structures associated with the DSF. A, B are the earliest brightenings. The box in **c** corresponds to the field of view of the partial frame images. In **d**–**g**, the arrow points to the long bright X-ray feature which moves out. Note that it has gone by 14:25:02 UT in **h**. In **i**, the numbers 1 and 2 are the locations of the centroids of the metric continuum emission. The vertical spikes in **g**–**i** are are due to saturation caused by the subflare.

quasi-stationary loops were responsible for most of the X-ray flux for several hours (at least until 18:00 UT), as in any typical long duration event and represent the third stage. Starting from the 14:10:06 UT image, we see that the X-ray emission from the AR increased rapidly which is due to the Hα subflare mentioned above. At the same time, several loops to the right of AR 7494 became very bright and was the dominant source of X-ray emission after $\sim$ 14:25 UT.

The field of view of the PFIs is represented by the box in Fig. 2c which encloses AR 7494. Notice that the PFI field of view also encloses the left end of the fast moving X-ray structure (marked by arrows in Fig. 2d-g). From the PFIs, we were able to determine the projected speed of the X-ray ejecta as $\sim$ 200 km s^{-1}. Taking into account of the location of the region (E20), we estimate that the deprojected speed of the loop to be $\sim$ 585 km s^{-1}. This is relatively a fast motion capable of driving a

shock wave in the corona. The different directions of the X-ray ejecta and the initial eruption may be significant in determining the conditions of shock formation. We shall return to this issue later in Sect. 4.1. There were a few additional loops that moved in the same direction as the main ejecta, but with slightly slower speeds. One of these can be seen in Fig. 2g directly to the south of the one pointed by arrow.

Two of the brightest LDE loop structures were also the sources of metric radio continuum emission. In the 14:27 UT image (Fig. 2i) we have marked the centroids (1, 2) of the radio continuum source as observed by the Nançay radioheliograph. Details of the radio continuum and its relation to soft X-ray emission can be found in Sect. 4.2. Since the first hint of soft X-ray activity usually starts around the time the filament lifts off, we infer that the DSF onset was around 13:30 UT as evident from the GOES plot (see Fig. 5).

The subflare in AR 7494 is clearly connected to the X-ray ejecta. It is not surprising because the active region is a part of the large-scale magnetic structure around the filament and hence is expected to participate in the eruption. There was also clear expansion of the AR to the NE which appears directly related to the eruption of the filament loops in the same direction. This feature can be seen in Fig. 2f-i.

2.3.2. Large-scale X-ray enhancement: a CME

What we described so far is the immediate vicinity of the DSF region. When we examined a larger area surrounding the filament, we found weak X-ray enhancements to the north and south of the LDE loops. Fig. 3 shows the evolution of this diffuse structure as a series of difference images. In Fig. 3a, we have drawn a box corresponding to the images shown in Fig. 2. We can see three active regions, two to the left and one to the right of the box. The images in Fig. 3a-b were subtracted from later images to reveal the weak X-ray enhancements. We have deliberately oversaturated the emission near the DSF region to bring out the diffuse emission. The diffuse enhancement starts almost at the same time as the initial loop brightenings (13:32:34 UT – Fig. 3c) observed close to the neutral line. The enhancement on the northern side is somewhat larger than that on the southern side. The overall latitudinal extent of the enhancement is more than 60°. There was no sign of the enhanced X-ray emission to the left of the two active regions located at the eastern end of the eruption region. The maximum extent of the X-ray enhancement was in the northeast direction from the DSF region. The enhancement seems to have structural complexity in the form of many linear structures. Since the filament erupted from close to the disk center (N00E10), we expect the associated CME to be roughly Earth-directed with a small eastward tilt.

We chose several locations (see Fig. 4) near the site of the DSF and in the surrounding areas to study the change in X-ray flux with time. A summary plot of X-ray fluxes at these locations is shown in Fig. 5. We have plotted the X-ray flux in sandwich filter normalized to the flux at the initial time (10:22:22 UT). The top panel of Fig. 5 shows the X-ray flux close to the initial location of the filament. A and B represent the light curves at locations where earliest X-ray changes were observed (see Fig. 2 (b)). L1 and L2 are the two brightest structures at the apex of which the metric continuum sources were located (see Fig. 2i). The X-ray flux at N1 and L2 can be seen to increase even before 14:00 UT. We have also plotted the normalized radio flux of the radio continuum at 164 MHz for comparison. In the bottom panel, we have shown the X-ray flux at locations (N1, N2, S1, S2) away from the site of filament disappearance. We notice that the flux on the northern side (N1, N2) of the plage region is always higher than that on the southern side (S1, S2). The locations are widely separated (almost a solar diameter in the north-south direction), but still the X-ray enhancement can be clearly noticed. Note that this size is comparable to the typical width of white light CMEs (see, e.g., Hundhausen, 1993). In the bottom panel, we have also plotted the flux at the core of an active region located to the left of the region of eruption (marked AR in Fig. 4) which remains rather flat. From the light curves obtained at more locations than marked in Fig. 4 we found that the changes can be found almost over the entire field of view to the right of AR. Interestingly, there is no significant enhancement to the left of AR except for the increase due to solar rotation above the limb (R in Fig. 4) and due to another eruption later on (around 18 UT). Comparing the top and bottom panels of Fig. 5 we see that the X-ray enhancement (LDE) in the vicinity of the initial filament location is much larger than at the surrounding locations (CME). The X-ray signature of CMEs is quite complex and is not fully established (see e.g., Hudson et al., 1996; Gopalswamy, 1999). In the present event, we can say that the large-scale diffuse enhancement is definitely a CME signature, although it could represent only a portion of the full CME that emits significantly in X-rays. Note that the large-scale diffuse enhancement and the LDE are two distinct signatures corresponding to the CME and the post-eruption arcade formation respectively.

There were no large-scale dimmings associated with this event. However, there were smaller dimming regions, such as the one in the region from where the structure B erupted (to the northeast of the AR 7494 in Fig. 3). There was another small dimming near the western end of the filament channel, the gap to the west of the bright loop marked '1' in Fig. 2i. These dimmings do indicate disappearance of some X-ray emitting structures, but not the full CME.

We need to be careful when interpreting the coordinated X-ray brightenings in a area as large as we see in our case, because there is a possibility that these low-level brightenings can be due to scattered light from much brighter loops. We have estimated the level of scattered light at various areas such as N1, using the formula for the SXT point spread function obtained by Hara et al. (1994), which shows that the scattering wing has the angular dependence of $r^{-2.0}$ without significant wavelength dependence. The calculation is based on short exposure images without saturation at the bright loops. We conclude that our large-area brightenings are much more intense than the estimated contributions of scattered light. For example, at N1, the observed intensity is about two orders of magnitudes larger than expected from scattered light. Residuals of correcting the stray-

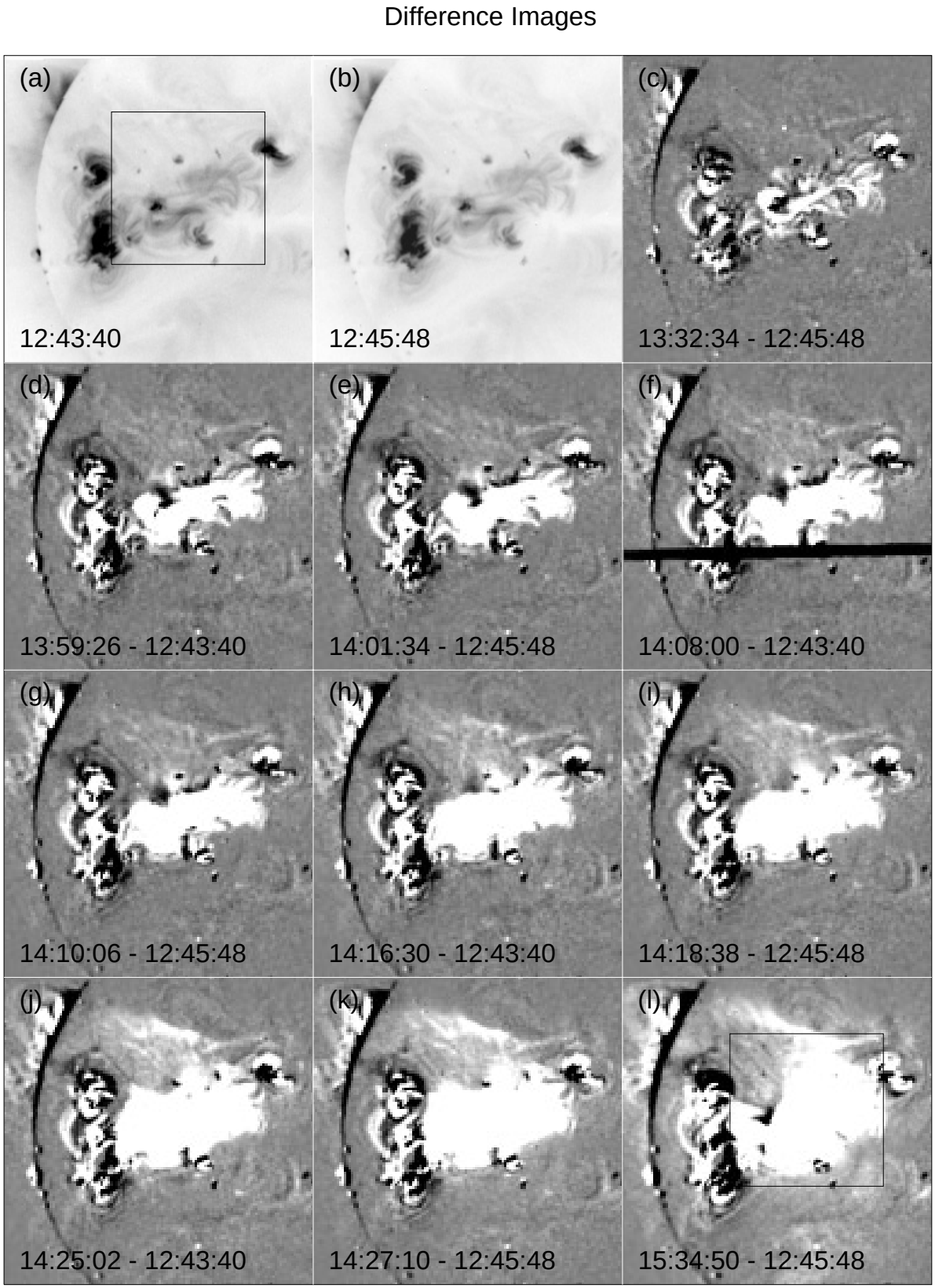

Fig. 3a–l. Evolution of the diffuse X-ray structure as a series of difference images **c**–**l**. The images at 12:43:40 **a** and 12:45:48 **b** were used as the pre-event images (shown in negative so darker regions correspond to higher in tensity) for subtraction. The box in (**a** and **l**) corresponds to the region shown in Fig. 2. The bright region in the middle of the figure is the LDE loops overexposed so that the diffuse enhancement could be seen better. The diffuse enhancement can be seen mostly to the north of the LDE loops and it is very weak on the southern side. The dark horizontal strip in **f** is due to a data gap.

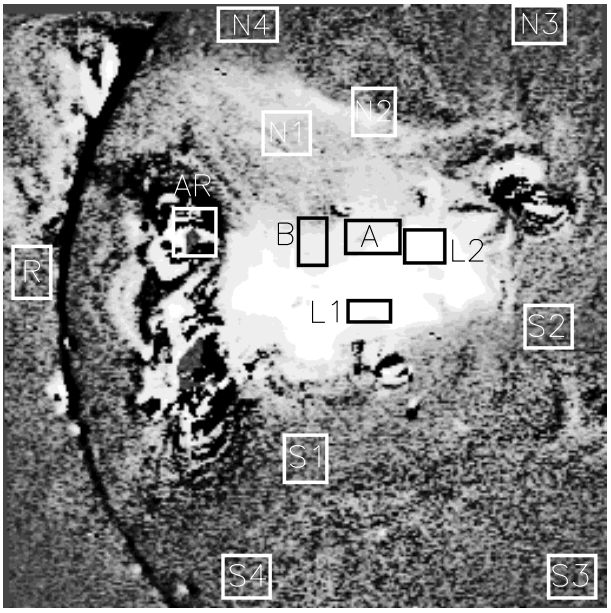

Fig. 4. Locations and areas of regions where X-ray fluxes were obtained. S and N denote regions to the south and north of the DSF. AR is a nearby active region to the east of the DSF. L1 and L2 are the two intense X-ray loop structures from which stationary continuum emission originated. A and B are the same as described in Fig. 2. X-ray emission from the reference region R was not affected by the large-scale eruption.

light (as a result of the optical light entering from an opening in the entrance filter) are also estimated to be negligible.

3. Temperature and emission measure analysis

We determined the temperature (T) and emission measure (EM) of the eruption region from the SXT/FFIs obtained in sandwich and thin aluminum filters. These filters are useful in providing line of sight averaged temperatures of non-flare plasmas. The images in the two filters had a separation of about 2 minutes and extrapolations were made to determine the filter ratios. We obtained the T and EM values at the locations marked in Fig. 4, averaged over the area of the boxes shown (area ~ 2.3 arcmin^2). We could not obtain meaningful values at locations far away from the eruption region because the signal was extremely weak. We discuss values obtained only from A, B, L1, L2, N1 and N2. In Fig. 6, we have plotted T and EM values obtained at the following locations (see Fig. 4): A, B (top), L1, L2 (middle) and N1, N2 (bottom). Fig. 6 essentially reflects the changes seen in Fig. 2 and 3. For instance, the first prominent peak in EM at location B corresponds to the passage of the loop structure marked by the arrow in Fig. 2. After the eruption of this loop, there was very little X-ray emission from region B and it was not possible to obtain meaningful values of T and EM. After about 16:00 UT, the formation of X-ray arcade extends to region B resulting in the second peak after 16:00 UT. At location A, there was high level of X-ray emission to begin with; later on, this structure disappeared due to the eruption and the emission due to rising arcade formation entered region A and was responsible for the later increase. We also see that the EM at N1 and N2 have a similar behavior and reflect the mass increase. The evolution of EM in L1 and L2 are similar except for the sharp peak in L2 corresponding to the GOES flare. The overall EM is higher close to the initial position of the filament (L1, L2). The temperature of the loops increased slightly during the main X-ray event (L1, L2) and remained roughly constant in N1 and N2. In Table 1, we have listed the maximum and minimum temperatures attained at each location. We see that the temperature increase is significant only in the vicinity of the eruptive filament.

Table 1. Minimum (T_{Min}) and maximum (T_{Max}) temperatures (MK) of the eruptive structures

Location	T_{Min}	T_{Max}
A	1.9	11.0
B	2.0	5.1
L1	1.8	6.2
L2	2.0	7.7
N1	1.8	2.3
N2	1.8	2.3

3.1. Temperature and EM for the flare region

The T and EM determined above are from the FFIs with a time resolution of up to $\sim$ 2 min. We also determined T and EM values from the PFI data (8 s cadence) taken in thin and thick aluminum filters. The locations chosen for T and EM analysis using the PFI data are shown in Fig. 7. FP1 and FP2 are two kernels which showed flare-like brightening. The linear structure extending from FP2 to the south also displayed some dramatic brightening and we have chosen a small area (C) of this structure for analysis. Material motion was seen to sweep through the entire PFI from the southwest to northeast and M is a representative location to describe this motion. A Comparison between PFIs and FFIs shows that the material motion is the same as the large-scale moving structure described in Fig. 2d-g. We measured the motion of X-ray ejecta along the path denoted by the arrow. The moving structure we analyzed in detail is marked X which is the same as the loop structure studied using FFIs (see Fig. 2d-g). L1 is the left end of the loop at the apex which the continuum radio source 1 was located (see Fig. 2i and Fig. 4).

The X-ray flux, T and EM at the chosen locations are plotted in Fig. 8. Though there is overall similarity, there are significant differences in the physical quantities at FP1 and FP2. It appears that they are two independent loops rather than the foot points of a single flare loop. The location C shows an increase in X-ray flux around 14:12 UT. By playing the X-ray images as movies, we found that the enhancement occurs when one of the moving X-ray structures arrives at the location of FP2. The moving X-ray structure seems to have triggered the sudden brightening of AR 7494 which consisted of FP1, FP2 and C. This can be seen in the top panel of Fig. 8. The flux at L1 (see Fig. 4) is not affected by the flare in AR 7494. The X-ray flux at M reaches a

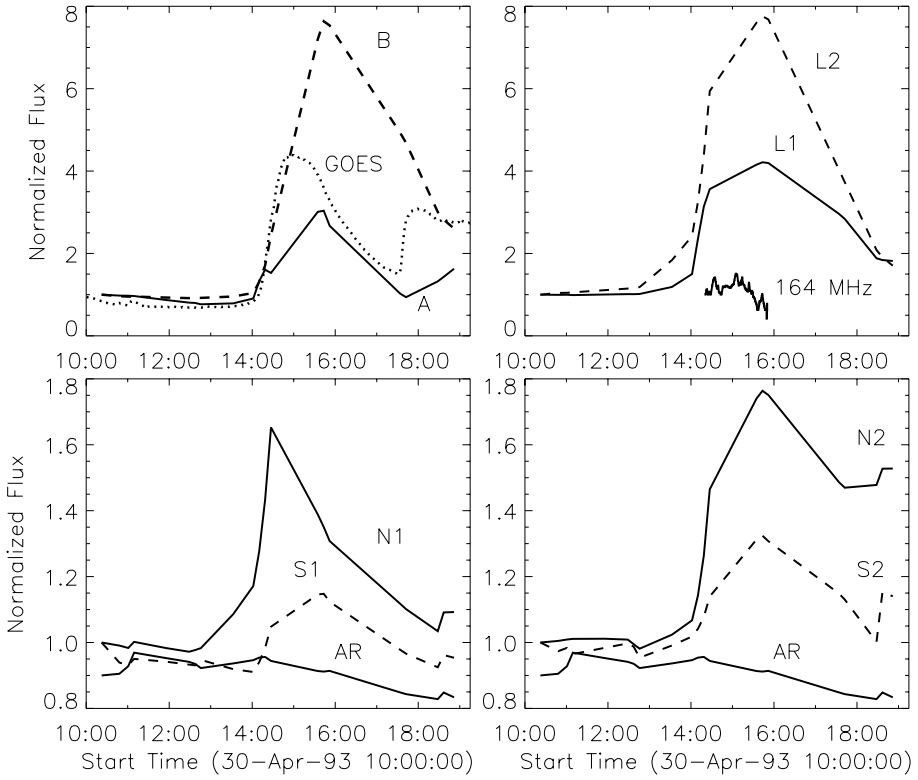

Fig. 5. X-ray flux at various locations marked in Fig. 4 showing that the large-scale X-ray enhancement is indeed a global phenomenon similar to a CME. The metric continuum radio flux at 164 MHz is also plotted along with the X-ray flux from the loop structures L1 and L2. Note that the reference region AR did not show any increase in X-ray flux. All the flux values are normalized to the corresponding values at 10:00 UT, except for the radio flux 164 MHz; it is normalized to the value at 14:19:43 UT. The GOES (1–8 Å) light curve is also shown for comparison. The second peak in the GOES plot is not related to this event. Note that the structures A and B show some dimming before 14 UT.

maximum at 14:12 UT (see Fig. 8). This means that most of the moving material had finished passing through the box M (see Fig. 7). The later enhancement at M is due to the slowly rising arcade formation following the eruption. The temperature at C also jumps at this time ($\sim$ 14:12 UT) from 4 MK to 6 MK after the arrival of hot material. The hot material passing through the box M had a temperature of about 6 MK, close to the value obtained from FFI images with different filters (see Table 1). Although FP1 and FP2 had the same initial temperature (4.5 MK), they attained different temperatures during the flare (5.3 MK for FP1 and 6.6 MK at FP2). Thus a detailed analysis of the X-ray data reveals that the Hα flare in AR 7494 was triggered by the X-ray ejecta sweeping past the active region.

4. Metric radio emissions

4.1. Coronal shock source for the type II burst

Metric type II bursts are thought to be due to fast mode MHD shock waves propagating through the corona. In this subsection, we attempt to identify the source of this shock wave. We shall consider two possible sources: the CME corresponding to the large-scale X-ray enhancement (Fig. 3), and the fast X-ray ejecta (X) described above (see Fig. 7).

As illustrated in Fig. 3(d), the large-scale X-ray enhancement can be seen as early as 13:59 UT at locations as far as half a solar radius in projection from the neutral line. Although we do not have positional information of the type II radio bursts, we do not expect the 36 MHz plasma level to be at a height larger than several tenths of a solar radius (see below for a coronal density model). Moreover, the metric type II burst starts only at 14:27 UT. This precludes the possibility of the type II burst being generated by a CME-driven shock.

Let us now consider the mass motion in the form of X-ray ejecta. We point out that, multiple structures were seen in motion and we shall consider the fastest one, marked B in Fig. 7. We measured the location of this structure along the path marked by an arrow in Fig. 7. We have assumed that the structure moved out radially and was inclined by an angle of $\sim 70^\circ$ from the plane of the sky. The resulting heliocentric distance of the ejecta is plotted in Fig. 9. The ejecta clearly accelerates, and a parabolic fit to the measured data points (the diamond symbols) gives an acceleration of $\sim$ 165 m s^{-2}. The fitted curve passes through the height measured from FFI at 14:18:38 UT. The speed of the ejecta at the time of the type II burst can be obtained from the fit as 672 km s^{-1}.

A disturbance will produce a shock ahead of it if the motion is super-Alfvenic. Close to the solar surface, the Alfven speed is high, so the X-ray ejecta is sub-Alfvenic. We can assume that the ejecta becomes super-Alfvenic when it reaches the 36 MHz plasma level where the type II burst starts in the second harmonic (at 72 MHz). The heliocentric distance attained by the ejecta can be obtained from the fit in Fig. 9 as 1.71 $R_\odot$. The density of the corona at the 36 MHz plasma level where the shock first forms can be obtained from the plasma frequency as $\sim 1.6\times10^7$ cm^{-3}. It looks promising that the X-ray ejecta indeed can be the source of the type II burst provided, its speed is consistent with the shock speed derived from the dynamic spectrum. The dynamic spectrum gives just the drift rate of the type II burst. We need a coronal density model to convert the drift rate into the speed of the shock.

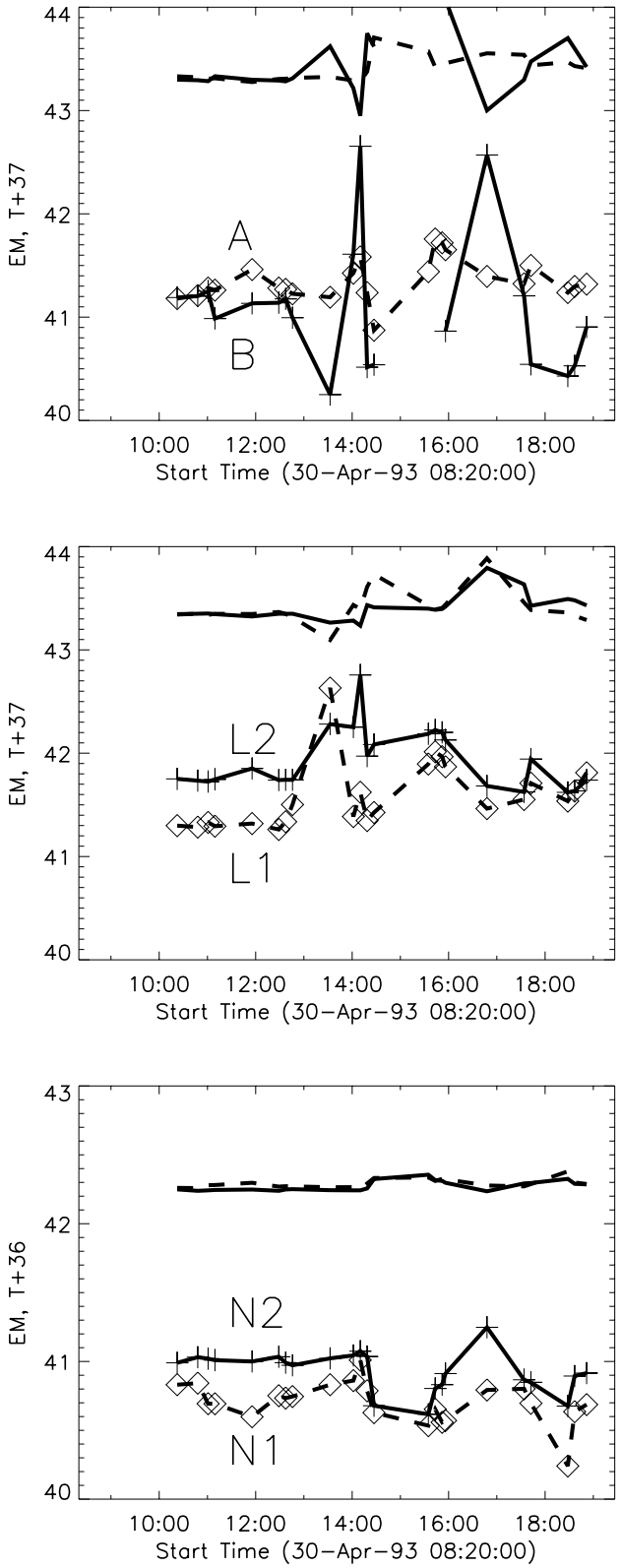

Fig. 6. Temperature (T) and emission measure (EM) values per pixel (in log units) obtained at A, B (*top*), L1, L2 (*middle*) and N1, N2 (*bottom*). Solid (dashed) curves correspond to locations B, L2, N2 (A, L1, N1). The T values are shifted by 36 units (*bottom panel*) and 37 units (*upper two panels*) to include T and EM on the same plot. The standard error bars on the T and EM plots were within a few percent.

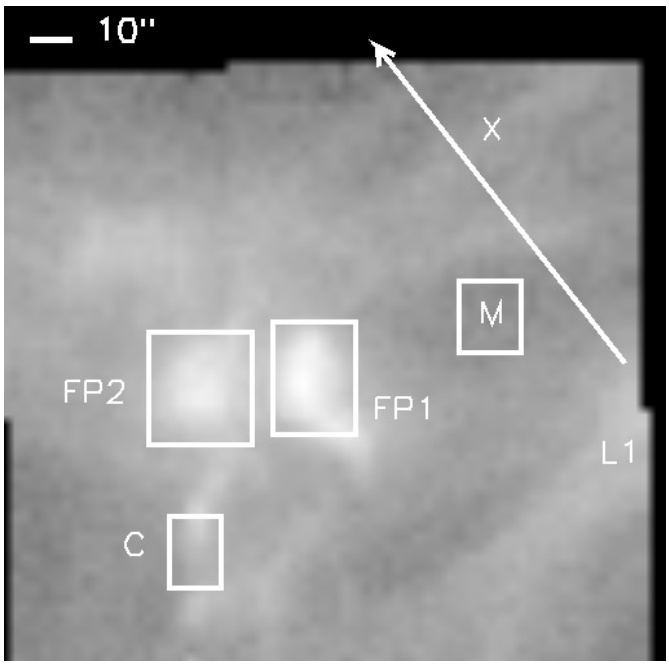

Fig. 7. Selected locations where T and EM were determined from the partial frame images (PFIs). The arrow denotes the path along which the motion of the X-ray ejecta (marked X) was measured. M is the region where we determined T and EM as plasma swept through. FP1 and FP2 are two bright kernels associated with the Hα flare in AR 7494. The region C showed impulsive changes associated with this flare. The south-eastern end of the loop L1 (see Fig. 4) lies within the PFI and is marked. The scale of the image is indicated at the top left.

The standard coronal density model used for this purpose is the Newkirk's model, n=4.2$\times 10^{4+4.32/r}$, where $n(r)$ = coronal density at a heliocentric height r expressed in units of solar radii. From this model, we can determine the heliocentric distance where the density is 1.6×10^7 cm^{-3} (corresponding to the 36 MHz plasma level) as 1.67 $R_\odot$. This is in excellent agreement with the distance (1.71 $R_\odot$) obtained from the dynamics of the X-ray ejecta. Thus we are justified in using Newkirk's model to get the speed (V_s) of the shock wave from the formula, V_s = $(L_n/f_p)df/dt$, where the coronal density scale height is given by, $1/L_n = n^{-1}(dn/dr)$, f_p is the plasma frequency (36 MHz) where the shock first forms and df/dt is the frequency drift rate of the type II burst, measured as 0.11 MHz s^{-1}. For r=1.67, we get L_n=0.28 $R_\odot$ so that the shock speed could be determined as 596 km s^{-1}, which is different from the velocity of the X-ray ejecta (V_X) only by $\sim$ 10%.

The only assumption we made in the above calculations is that the X-ray ejecta had a radial propagation. Since this was the only fast ejection during the appropriate time window of the event, we believe we have definite identification of the coronal shock source. This is a further confirmation of the result reported previously for the July 31, 1994 event where position information was available for the type II burst (Gopalswamy et al. 1997b). It must be pointed out that the Newkirk's model used here applies to a quiet corona in the equatorial region. We have a dynamic situation here involving a CME which can substan-

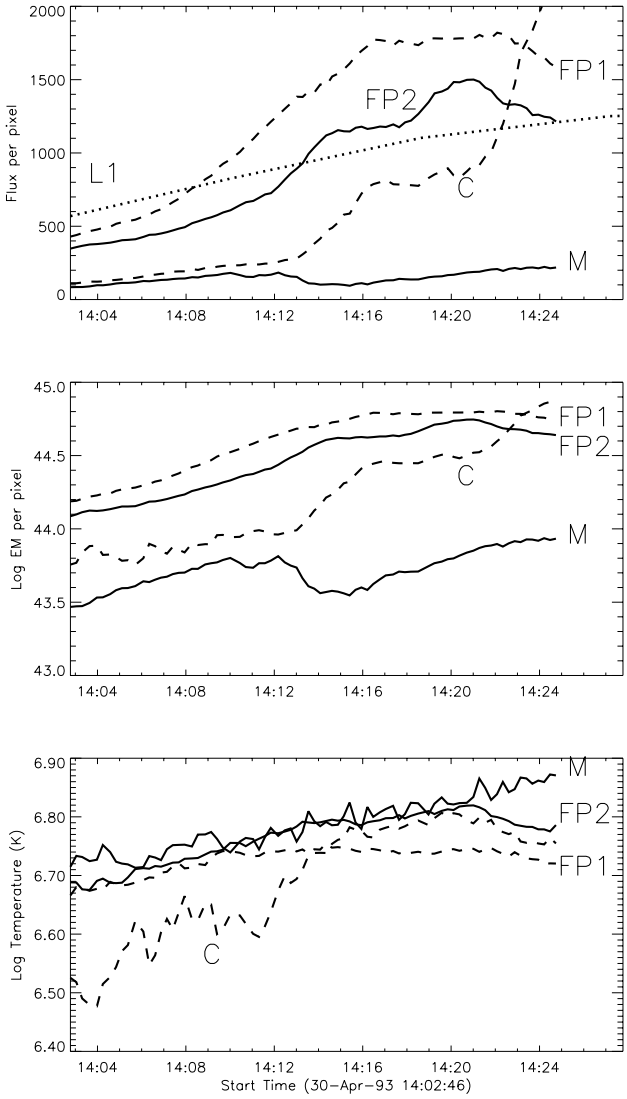

Fig. 8. X-ray flux, T and EM at locations FP1, FP2, M and C marked in Fig. 7. In the top panel the flux at the loop L1 (see Fig. 4) is also included for comparison. Note that the flux at L1 increases steadily, with no specific change at the time of the flare in AR 7494.

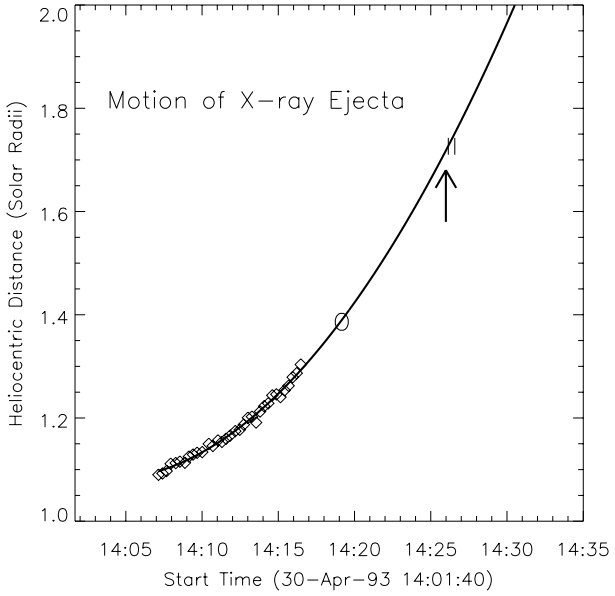

Fig. 9. Height-time plot of the X-ray ejecta fitted to the data points (diamonds) measured from the PFIs. The open circle denotes the data point obtained from the FFI. The location of the type II is marked 'II' and pointed by the arrow.

tially alter the conditions of the background corona and hence the derived speed of the coronal shock may not be accurate. Moreover, the ability of the X-ray ejecta to drive a shock also depends on the background flow speed modulated by the CME.

An important result of this study is that the X-ray ejecta occurs after the initial eruption (the CME) of the X-ray arcade overlying the filament. The relationship between the Hα filament and the X-ray ejecta cannot be determined here due to lack of observations. However, the eruption of the confining structure B (seen in Fig. 2) clearly precedes the X-ray ejecta as in the scenario proposed by Moore et al. (1997).

4.2. Continuum radio emission

The metric continuum associated with the two bright X-ray loops was extremely weak and was present briefly between 14:00 and 15:00 UT (see Fig. 5). The peak flux was only ~ 0.09 sfu at 14:29 UT. The gradual enhancement is most likely the free-free emission from the X-ray emitting plasma. To see this, we derive the temperature and emission measure of the X-ray emitting structures and compute the expected radio brightness temperature. At the time of the peak radio emission, we derived the temperature of the plasma to be about 2.5 MK. The emission measure per pixel averaged over the area indicated in Fig. 4 is $\sim 2.69 \times 10^{44}$ cm^{-3} which gives a column emission measure of $\sim 2.12 \times 10^{27}$ cm^{-5}. The standard formula for optical depth (τ_{ff}) due to free-free emission is,

$$\tau_{ff} = 0.2\, EM f^{-2} T^{-1.5}, \quad (1)$$

where EM is the column emission measure, f is the observing frequency and T is the plasma temperature. For the above value of T and EM, τ_{ff} at 164 MHz becomes ~ 4 so that the X-ray emitting plasma is marginally optically thick. The resulting radio brightness temperature is ~ 2.5 MK.

The Nançay Radioheliograph provided only the centroid of the radio source and we do not have the source size to determine the brightness temperature from the radio observations. However, we can determine the required radio source size from the radio brightness temperature (T_b) obtained from X-ray observations and the radio flux (S) using the relation,

$$T_b = 8.5 \times 10^{23} S \theta^{-2} f^{-2}, \quad (2)$$

where θ is the source size in arc minutes. Using the observed values (S=.09 sfu, T_b=2.5 MK) we get θ=1.1 arc min. This is roughly the size of the loop at its top and hence is consistent with the interpretation of free-free emission form the X-ray emitting plasma. At later times, the temperature increased by a factor of 3 and the X-ray loop becomes optically thin, resulting in very

little radio flux. Observation of the free-free emission from the X-ray loops associated with the filament eruption may be of interest in detecting low temperature X-ray arcade formation following filament eruptions/CMEs.

5. Discussion

The present study is an important addition to our previous studies on the coronal changes associated with filament eruptions. Although we did not have good observational coverage of the filament itself, we had detailed information of the event from X-ray observations. There were three types of X-ray signatures associate with the eruption: the diffuse enhancement (the CME), the LDE arcade and the X-ray ejecta. In addition, there was a Hα subflare in AR 7494 triggered by mass motions associated with the filament eruption (see also Khan et al., 1994; 1997). The X-ray flux due to the Hα flare itself is very small compared to the LDE originating from loops associated with the filament eruption. The Hα flare occurred almost an hour after the onset of the soft X-ray signatures of the eruption.

There is no clear dimming signature in this event. If material expands towards the observer, we do not expect a coronal dimming because the X-ray emitting material is simply displaced along the line of sight. However we do see changes which represent motion of X-ray emitting structures in and out of particular locations. The compact dimmings due to the eruption of pre-event structures (A and B in Fig. 5) are of this kind.

We examined the Dst index for next several days and we did not find any geomagnetic storms. The magnetogram in Fig. 1e suggests that the vertical component of the magnetic field approaching the earth is predominantly northward which may be one of the reasons why there was no geomagnetic storm (McAllister et al., 1996; Khan et al., 1997).

The radio signature of arcade formation seems to be a stationary continuum at metric wavelengths. It is important to note that the metric continuum is thermal emission, contrary to the nonthermal continua of various kinds studied in the past. However, there were not many simultaneous imaging observations in radio and X-rays. The identification of stationary thermal continuum at metric wavelength needs to be explored further as a possible indicator of coronal arcade formation without significant particle acceleration. The arcade formation has been observed in microwaves before (Hanaoka et al., 1994), but this is the first report at metric wavelengths.

The identification of the type II burst with a shock driven by the X-ray ejecta has also important implications for understanding coronal shock sources. The coronal shocks inferred from metric type II bursts are attributed to flares and CMEs (see e.g., Gopalswamy et al., 1998b; Kaiser et al., 1998). We have attempted to identify the driver as the X-ray ejecta which is particular aspect of the eruptive event. This is somewhat similar to the 1994 July 31 event reported in a previous study (Gopalswamy et al., 1997b), where we showed that short-lived X-ray ejecta following CMEs may be a source of the coronal shocks. Since we inferred that the X-ray ejecta was preceded by a CME, we need to consider the possibility of the X-ray ejecta moving in the wake of the CME. We need a detailed spatial relationship between the X-ray ejecta and the CME to pursue this further.

6. Conclusions

We have studied a filament disappearance event and the associated changes in the surrounding coronal medium in X-rays. The pre-eruption state of the region consisted of a dark filament with an overlying arcade observed in X-rays. Without the X-ray images, the event would look like a thermic disparision brusque. A detailed analysis revealed that diffuse X-ray emission was present covering a large area of the solar disk around the eruptive filament. The active regions located near-by seem to have acted like solid walls that did not let the eruption signatures go past them.

The X-ray emission from the eruptive event consisted of three different components: (i) A large-scale X-ray enhancement which seems to be the X-ray counterpart of a CME originating in the vicinity of the initial filament location, (ii) fast X-ray ejecta in the form of long loop-like structures that accelerated outward with very high speeds (~ 670 km s^{-1} at a height of 0.7 $R_\odot$), and (iii) quasi-stationary X-ray loops in the vicinity of the DSF region which represent the classical LDE emission. The dynamics of the CME-like material could not be studied very well. Unfortunately, there was no coronagraph operating at this time and hence we were not able to confirm if there was a white light CME associated with the filament disappearance.

We suggest that the fast X-ray ejecta is the source of the coronal shock that produced the metric type II burst. The quasi-stationary structures (LDE) in the vicinity of the DSF region constitute the arcade formation now well-known from many Yohkoh X-ray events. These loops are dense enough to be optically thick at metric radio waves and hence their thermal free-free emission could be detected as a stationary radio continuum.

Acknowledgements. NG was supported by NASA grants NAG-5-6139 and NAG-5-7238. NN was supported by NASA grant NAS8-40108. We thank P. Zarka for providing information on the type II burst from the Nançay Decametric Array. The NSO/Kitt Peak data used here were produced cooperatively by NSF/NOAO, NASA/GSFC and NOAA/SEC. The authors thank the referee A. H. McAllister for critical comments which helped us improve the presentation of the paper.

References

Gopalswamy N., 1999, In: Bastian T., Gopalswamy N., Shibasaki K. (eds.) Solar Physics from Radio Observations. In press

Gopalswamy N., Kundu M.R., Hanaoka Y., et al., 1996, New Astron. 1, 207

Gopalswamy N., Hanaoka Y., 1998, ApJ 498, L179

Gopalswamy N., Hanaoka Y., Kundu M.R., et al., 1997a, ApJ 475, 348

Gopalswamy N., Kundu M.R., Manoharan P.K., et al., 1997b, ApJ 486, 1036

Gopalswamy N., Hanaoka Y., Lemen J.R., 1998a, In: Webb D., Rust D., Schmieder B. (eds.) Proc. IAU Colloquium 167, PASP Conf. Series, p. 358

Gopalswamy N., Kaiser M.L., Lepping R.P., et al., 1998b, JGR 103, 307

Hanaoka Y., Kurokawa H., Enome S., et al., 1994, PASJ 46, 205
Hara H., Tsuneta S., Acton L.W., et al., 1994, PASJ 46, 493
Hudson H.S., Acton L.W., Freeland S.L., 1996, ApJ 470, 629
Hudson H., Webb D.F., 1997, In: Crooker N., Joselyn J.A., Feynman J. (eds.) Coronal Mass Ejections. AGU Monograph 99, p. 27
Hundhausen A.J., 1993, JGR 98, 13177
Joselyn J.A., McIntosh P.S., 1981, JGR 86, 4555
Kahler S.W., 1977, ApJ 214, 891
Kaiser M.L., Reiner M.J., Gopalswamy N., et al., 1998, GRL 25, 2501
Khan J.I., Uchida Y., McAllister, Watanabe Ta., 1994, In: Uchida Y., Watanabe T., Shibata K., Hudson H.S. (eds.) X-ray Solar Physics from Yohkoh. p. 201
Khan J.I., Uchida Y., McAllister A.H., et al., 1997, A&A 336, 753
McAllister A.H., Kurokawa H., Shibata K., Nitta N., 1996, Solar Phys. 169, 123
McAllister A.H., Uchida Y., Tsuneta S., et al., 1992, PASJ 44, L205
Moore R.L., Schmieder B., Hathaway D.H., Tarbell T.D., 1997, Solar Phys. 176, 153
Mouradian Z., Martres M.J., Soru-Escaut I., 1986, In: Poland A. (ed.) Coronal and Prominence Plasmas. p. 221
Sheeley N.R., Bohlin J.D., Brueckner G.E., et al., 1975, Solar Phys. 45, 377
Solberg F.C.R., McAllister A., 1998, In: Webb D., Rust D., Schmieder B. (eds.) Proc. IAU Colloquium 167, PASP Conf. Series, p. 171
Tsuneta S., Acton L., Bruner M., et al., 1991, Solar Phys. 136, 37
Wagner W.J., 1986, In: Poland A. (ed.) Coronal and Prominence Plasmas. p. 215